

Origins of Irreversibility in Layered $\text{NaNi}_x\text{Fe}_y\text{Mn}_z\text{O}_2$ Cathode Materials for Sodium Ion Batteries

Changjian Deng, Eric Gabriel, Paige Skinner, Sungsik Lee, Pete Barnes, Chunrong Ma, Jihyeon Gim, Miu Lun Lau, Eungje Lee,* and Hui Xiong*



Cite This: <https://dx.doi.org/10.1021/acsami.0c13850>



Read Online

ACCESS |



Metrics & More



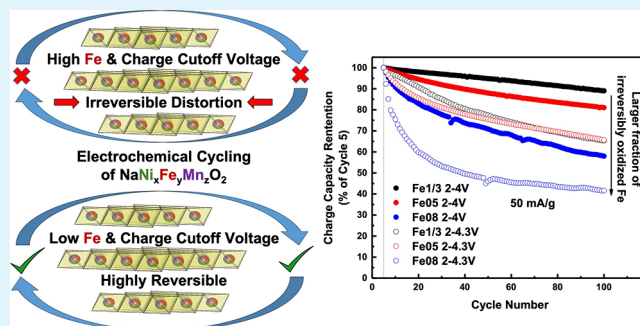
Article Recommendations



Supporting Information

ABSTRACT: Layered $\text{NaNi}_x\text{Fe}_y\text{Mn}_z\text{O}_2$ cathode (NFM) is of great interest in sodium ion batteries because of its high theoretical capacity and utilization of abundant, low-cost, environmentally friendly raw materials. Nevertheless, there remains insufficient understanding on the concurrent local environment evolution in each transition metal (TM) that largely influences the reversibility of the cathode materials upon cycling. In this work, we investigate the reversibility of TM ions in layered NFMs with varying Fe contents and potential windows. Utilizing *ex situ* synchrotron X-ray absorption near-edge spectroscopy and extended X-ray absorption fine structure of precycled samples, the valence and bonding evolution of the TMs are elucidated. It is found that Mn is electrochemically inactive, as indicated by the insignificant change of Mn valence and the Mn–O bonding distance. Fe is electrochemically inactive after the first five cycles. The Ni redox couple contributes most of the charge compensation for NFMs. Ni redox is quite reversible in the cathodes with less Fe content. However, the Ni redox couple shows significant irreversibility with a high Fe content of 0.8. The electrochemical reversibility of the NFM cathode becomes increasingly enhanced with the decrease of either Fe content or with lower upper charge cutoff potential.

KEYWORDS: layered transition-metal oxide cathode, reversibility, local environment evolution, X-ray absorption spectroscopy, sodium ion battery



1. INTRODUCTION

Large-scale energy storage systems (ESSs) have become extremely important for the penetration and utilization of intermittent renewable energy sources for the electrical grids.¹ Among different types of ESSs, rechargeable battery technology is attractive because of its high round-trip efficiency, long cycle life, and low maintenance.² Lithium ion batteries (LIBs) have dominated the rechargeable battery market for decades. However, surging demand for LIBs in the automotive electric vehicle market amid limited and geographically constrained lithium mineral reserves has driven up the price. Therefore, there is an urgent need to develop low-cost and highly stable rechargeable battery technologies based on abundant resources. Among all candidates, the sodium ion battery, manufactured with low cost and abundant raw materials, is promising because of similar chemistry and technology as LIBs.^{2–7} In terms of cathode materials for sodium ion batteries, layered O3-type $\alpha\text{-NaFeO}_2$ is of great interest because of its high theoretical capacity and utilization of abundant, low-cost, environmentally friendly raw materials.³ The electrochemical performance of NaFeO_2 can be significantly improved through substitution of Fe ions by other transition metals (TMs).⁴ Although various TMs have been studied as the dopants,

substitution of nickel and manganese ions is particularly attractive. Kim et al. reported $\text{NaNi}_{1/3}\text{Fe}_{1/3}\text{Mn}_{1/3}\text{O}_2$ cycled within a voltage window of 1.5–4.0 V.⁵ The cathode exhibited an average voltage of 2.75 V, a moderate capacity of 100 mA h g^{-1} for 150 cycles, and a capacity of 94 mA h g^{-1} at 1 C.⁵ Yabuuchi et al. investigated the influence of various Fe contents in a $\text{NaFe}_x(\text{Ni}_{0.5}\text{Mn}_{0.5})_{1-x}\text{O}_2$ system where $x = 0, 0.2, 0.4, 0.6, 0.8,$ and 1 .⁶ The lattice parameters a and c increased linearly with the increase of Fe content.⁶ $\text{NaFe}_{0.4}\text{Ni}_{0.3}\text{Mn}_{0.3}\text{O}_2$ showed increased electrochemical performance, delivering 130 mA h g^{-1} reversible capacity in a voltage range of 2.0–3.8 V.⁶ Meanwhile, Yuan et al. conducted a study on a similar system, $\text{NaFe}_x(\text{Ni}_{0.5}\text{Mn}_{0.5})_{1-x}\text{O}_2$ where $x = 0, 0.1, 0.2, 0.3, 0.4,$ and 1 .⁷ The cathode with Fe = 0.2 showed a reversible capacity of 125 mA h g^{-1} after 30 cycles and a high capacity of 86 mA h g^{-1} at 10 C rate within a potential window of 2.0–4.0 V.⁷ Wang et al.

Received: August 1, 2020

Accepted: October 14, 2020

investigated commercial $\text{NaNi}_{1/3}\text{Fe}_{1/3}\text{Mn}_{1/3}\text{O}_2$ cathode materials.⁸ The synthesis process was scaled up by using hydroxide coprecipitation followed by solid state reaction, and the cathode exhibited a capacity of 125 mA h g^{-1} at 1 C .⁸ The electrochemical performance at various operating temperatures was also evaluated.⁸ Moreover, a soft packed large-scale 1 Ah battery with $\text{NaNi}_{1/3}\text{Fe}_{1/3}\text{Mn}_{1/3}\text{O}_2$ as the cathode and hard carbon as the anode was prepared and maintained 0.73 Ah after 500 cycles at 1 C .⁸ In addition to the electrochemical performance, the evolution of the crystallographic structure was investigated. Xie et al. conducted operando X-ray diffraction (XRD) on the $\text{NaFe}_{1/3}\text{Ni}_{1/3}\text{Mn}_{1/3}\text{O}_2$ cathode with the voltage window of $2.0\text{--}4.3 \text{ V}$ and discovered a highly reversible phase transformation path, $\text{O3--P3--O3'--P3--O3}$, during the charge and discharge process.⁹

Although the electrochemical performance and the phase transition in the layered cathodes have been widely studied, the local evolution of TM ions in terms of valence and bonding structure is seldom explored. TMs play a significant role in layered cathode materials in terms of charge compensation, average potential, air stability, and structural stability. First, TMs serve as redox couples to account for the capacity in the electrodes through charge compensation mechanism.^{10,11} For example, $\text{Ni}^{2+}/\text{Ni}^{4+}$ redox couple can contribute twice the capacity of the $\text{Fe}^{3+}/\text{Fe}^{4+}$ couple in theory because of two-electron transfer of $\text{Ni}^{2+}/\text{Ni}^{4+}$ over one-electron transfer of $\text{Fe}^{3+}/\text{Fe}^{4+}$. Second, the electrode potential is dependent on the valence state, ionic radius, electronegativity, and the local environment of the cations in electrode materials of interest.¹² The more energy released when electrons are inserted into TM orbitals, or the more the energy consumed when electrons are promoted from TM orbitals, the higher the electrode potential of the electrode materials.¹² Third, the air stability of layered cathodes can be significantly improved by TM substitution. Water molecules in air can easily incorporate into the Na layer of layered cathodes, leading to expansion of interlayer spacing, formation of impure phases, and consequently, electrode instability in air.¹³ It has been reported that the substitution of Cu ions achieves high air/moisture stability.^{13,14} Yao et al. reported the substitution of Cu can decrease the interlayer distance to prevent the insertion of water molecules.¹⁴ Lastly, the structural stability of the electrode is significantly influenced by the TMs via Jahn–Teller distortion or TM migration.¹⁵ Ni^{3+} , Mn^{3+} , and Fe^{4+} are ions with strong Jahn–Teller effect that increases the electronic localization and decreases sodium ion diffusion.¹⁵ Furthermore, it has been proposed that the migration of Fe ions from octahedral sites in the TM layer to tetrahedral sites in the sodium layer may lead to detrimental structural and capacity fade in the layered cathodes.^{4,16} Although TM ions have massive influence on layered cathode materials in various aspects, to the best of our knowledge, concurrent evolution of the local environment in each TM ion within $\text{NaNi}_x\text{Fe}_x\text{Mn}_x\text{O}_2$ cathodes has not been investigated.

Here, we investigate a $\text{NaFe}_x(\text{Ni}_{0.5}\text{Mn}_{0.5})_{1-x}\text{O}_2$ system, where $x = 1/3, 0.5,$ and 0.8 , systematically to elucidate the simultaneous evolution of the local environment of each TM ion (Ni, Fe, and Mn) in various cation compositions and different charge cutoff potentials (i.e., 4.0 vs 4.3 V). The molar ratio of Na and TM ions is confirmed by inductively coupled plasma mass spectroscopy (ICP–MS). The crystal structures of all samples are determined by XRD and Rietveld refinement where an O3-type layered $\alpha\text{-NaFeO}_2$ structure (space group:

$\bar{R}3m$) is obtained. *Ex situ* synchrotron X-ray absorption near edge spectroscopy (XANES) and extended X-ray absorption fine structure (EXAFS) are conducted in precycled samples to elucidate the evolution of the TM valence state and local bonding structure. The electrochemical reversibility of the cathode becomes increasingly enhanced with the decrease of either Fe content or with lower upper cutoff potential.

2. EXPERIMENTAL SECTION

2.1. Synthesis. The nominal $\text{NaNi}_{1/3}\text{Fe}_{1/3}\text{Mn}_{1/3}\text{O}_2$ (NFM– $\text{Fe}_{1/3}$), $\text{NaNi}_{0.25}\text{Fe}_{0.5}\text{Mn}_{0.25}\text{O}_2$ (NFM– $\text{Fe}_{0.5}$), and $\text{NaNi}_{0.1}\text{Fe}_{0.8}\text{Mn}_{0.1}\text{O}_2$ (NFM– $\text{Fe}_{0.8}$) cathodes were synthesized by the solid-state reaction.⁵ For each cathode, an aqueous solution with the desired stoichiometric amount of nickel sulfate, iron sulfate, and manganese sulfate was added into a solution of sodium oxalate under stirring. The coprecipitation solution was continuously stirred for 3 h at $70 \text{ }^\circ\text{C}$ in air. The product was filtered, washed, and dried. The dried precursor powder and sodium carbonate were manually grinded with a mole ratio of 2:1.05 to compensate the Na loss as vapor at high temperatures.⁸ The mixed powder was pressed into pellets and calcined at $850 \text{ }^\circ\text{C}$ for 12 h in air. It was then cooled down and stored in a glove box.

2.2. Materials Characterization. The composition in each cathode was determined by ICP–MS (iCAP 6000 Radial, Thermo Fisher Scientific Inc.). The morphology of the samples was examined by scanning electron microscopy (SEM, Sirion 200, FEI Company). The crystal structures of the pristine materials were determined by XRD (Rigaku Miniflex 600) with filtered $\text{Cu K}\alpha$ radiation ($\lambda = 1.5418 \text{ \AA}$) from 5 to 120° with a step of 0.01° and scan rate of $0.8^\circ/\text{min}$. The patterns were analyzed by the general structure analysis system package.¹⁷ The cycled electrodes tested with X-ray absorption spectroscopy (XAS) were immediately disassembled and washed with dimethyl carbonate in a glove box once five precycles were finished. Then, they were carefully sealed using the Kapton tape to avoid contact with air. XAS was conducted at the Advanced Photon Source at Argonne National Lab at beamline 12-BM. XANES data were collected in fluorescent mode and analyzed by the Athena program using the IFEFFIT package.¹⁸ The reference spectra of Ni, Fe, and Mn foil were collected simultaneously with each sample for energy calibration and data alignment. The normalized EXAFS spectra were converted from energy to wave vector k and then weighted by k^3 . The crystallographic information for EXAFS fitting is built up by the results of Rietveld fitting of XRD.

2.3. Electrochemistry. All laminated electrodes were prepared by mixing 80% active materials, 10% super carbon C45 (Timcal America Inc.), and 10% poly(vinylidene fluoride), and then, the slurry was screen-printed by a compact tape casting coater (MTI Corp) on an aluminum current collector. The electrodes were punched into discs with a loading density of $\sim 2.7 \text{ mg cm}^{-2}$. The half-cells were prepared with the cathode, glass fiber separators (Fisher Scientific), and a sodium counter electrode (Sigma-Aldrich) in an electrolyte of 1 M NaPF_6 (Alfa Aesar) in propylene carbonate (BASF). The coin cells were cycled on an Arbin battery tester with the potential window of $2.0\text{--}4.0$ and $2.0\text{--}4.3 \text{ V}$. The cycle life and voltage profile studies were conducted at the current rate of 50 and 12 mA g^{-1} , respectively.

3. RESULTS AND DISCUSSION

ICP–MS analysis confirms the composition of NFM– $\text{Fe}_{1/3}$, NFM– $\text{Fe}_{0.5}$, and NFM– $\text{Fe}_{0.8}$ to be $\text{Na}_{1.048}\text{Ni}_{0.346}\text{Fe}_{0.330}\text{Mn}_{0.324}\text{O}_2$, $\text{Na}_{1.064}\text{Ni}_{0.259}\text{Fe}_{0.498}\text{Mn}_{0.243}\text{O}_2$, and $\text{Na}_{1.070}\text{Ni}_{0.113}\text{Fe}_{0.791}\text{Mn}_{0.096}\text{O}_2$, respectively, which is consistent with the expected stoichiometry within acceptable error. The morphologies of the samples are characterized by SEM (Figure S1, Supporting Information). All samples exhibit a mixture of microscale particles and flakes with uniform size. The powder XRD patterns of NFM– $\text{Fe}_{1/3}$, NFM– $\text{Fe}_{0.5}$, and NFM– $\text{Fe}_{0.8}$ are shown in Figure S2 (Supporting Information).

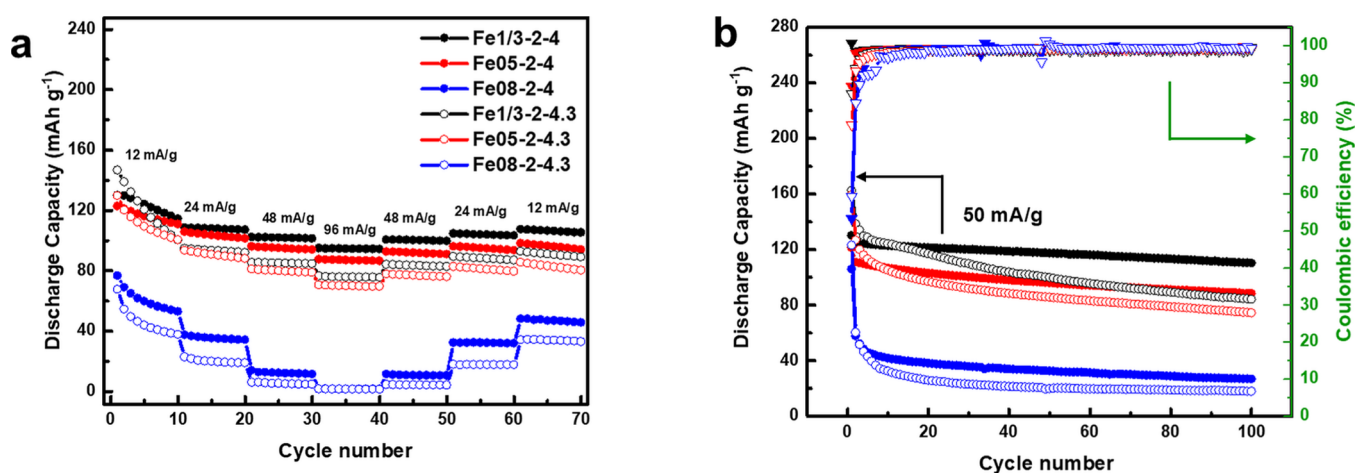


Figure 1. (a) Rate study and (b) cycle life shown in charge capacity of NFM-Fe_{1/3}, NFM-Fe_{0.5}, and NFM-Fe_{0.8} samples.

All samples can be indexed to the space group $R\bar{3}m$ with the α -NaFeO₂ structure. Rietveld refinement is conducted to extract detailed crystal structure information of the samples. The refinement results are summarized in Table S1 (Supporting Information). The details of Rietveld refinement can be found in Table S2 (Supporting Information). The lattice constant a and c (Figure S3, Supporting Information) increase with the increase of Fe content, suggesting the formation of a solid solution of Ni- and Mn-substituted α -NaFeO₂, consistent with previous studies.^{6,7}

The rate capability and cycle life study of NFM-Fe_{1/3}, NFM-Fe_{0.5}, and NFM-Fe_{0.8} samples are evaluated in the potential windows of 2.0–4.0 and 2.0–4.3 V (Figure 1). Fe1/3-2-4, Fe05-2-4, and Fe08-2-4 represent the cathode samples cycled with a potential window of 2.0–4.0 V, while Fe1/3-2-4.3, Fe05-2-4.3, and Fe08-2-4.3 represent samples cycled in a potential window of 2.0–4.3 V. In general, both cycle life and rate capability of the samples improve with either a lower upper charge cutoff potential window (2.0–4.0 V) or less Fe content. Under the same TM composition, cycling in the higher upper cutoff potential window (2.0–4.3 V) offers higher specific capacity during the first few cycles. However, the capacity quickly fades and eventually drops to a lower capacity than that of the samples cycled in a window of 2.0–4.0 V. Within the same potential window, both cycle life and rate capability of NFM-Fe_{1/3} show slightly higher capacity than that of NFM-Fe_{0.5} and significantly higher capacity than that of NFM-Fe_{0.8}. All samples show limited first-cycle Coulombic efficiency (CE), possibly because of irreversible phase transition to distorted O3' phase or cathode electrolyte interphase formation at high potential.^{9,19} In addition, the CE follows the trend that both a lower upper cutoff potential window and less Fe content can significantly improve the first cycle CE.

In order to separately investigate the effect of the potential window and TM composition on the reversibility, Fe1/3-2-4.3, Fe1/3-2-4, and Fe08-2-4 samples are selected, where Fe1/3-2-4.3 and Fe1/3-2-4 have the same TM composition, and Fe1/3-2-4 and Fe08-2-4 have the same potential window. The voltage profiles of Fe1/3-2-4.3, Fe1/3-2-4, and Fe08-2-4 in the first, second, and fifth cycle and the corresponding dQ/dV plots are shown in Figure 2. The Fe1/3-2-4.3 sample shows two plateaus in the voltage profile (Figure 2a) and two pairs of corresponding redox peaks in the dQ/dV plot (Figure 2b).

One peak pair locates in the low-voltage range (2.75–3.0 V) and the other at the high-voltage range (3.75–4.15 V). In terms of structural evolution, the pairs at the low and high voltages can be related to the phase transition between O3–P3 and P3–O3', respectively.^{7,9} The sloping profile between the two plateaus is associated with the solid–solution reaction within the P3 phase.^{7,9} The first cycle charge capacity of Fe1/3-2-4.3 is 226 mA h g⁻¹, consistent with the theoretical capacity (240 mA h g⁻¹) calculated based on the charge compensation of Ni²⁺/Ni⁴⁺ and Fe³⁺/Fe⁴⁺ redox pairs. The voltage profile and dQ/dV plot of the Fe1/3-2-4 sample are shown in Figure 2c,d, respectively. There is only one apparent plateau in the discharge voltage profile (Figure 2c), which corresponds to the peak at 2.75 V in the dQ/dV plot (Figure 2d). This is attributed to the structural transition from O3 to P3.^{7,9} Note that there is a small onset peak at the end of the charge process (4.0 V) in the dQ/dV plot, suggesting the phase transition to O3'.¹⁰ The Fe1/3-2-4 sample delivers 138 mA h g⁻¹ capacity in the first charge, slightly smaller than the theoretical capacity of 161 mA h g⁻¹ based on the Ni²⁺/Ni⁴⁺ redox. The voltage profile and dQ/dV plot of the Fe08-2-4 sample are shown in Figure 2e,f, respectively. There is a reduction peak at 3.20 V and an oxidation peak at 3.35 V in the dQ/dV plot (Figure 2f). The redox peaks at 3.20 and 3.35 V of the Fe0.8-2-4 sample are consistent with the plateau of the α -NaFeO₂ cathode.¹⁶ It is concluded that both NFM-Fe_{1/3} samples with different potential windows show a similar O3–P3 phase transition. When the cutoff voltage increases from 4 to 4.3 V, the P3–O3' phase transition gets activated. It is noted that there is a small voltage jump in the first charge of the electrodes. The voltage spike in the initial cycle is possibly associated with surface activation, where the surface impedance needs to be overcome.^{20,21} It is possible that the samples had some Na precursor residues left at the surface, which caused the spike.

Ex situ synchrotron XAS is conducted to investigate the local chemical and structural environment of TMs at various states of charge (SOCs) such as SOC_0%, SOC_33.3%, SOC_66.7%, and SOC_100%. The voltages related to the specific SOC in each sample are shown in Figure 3. All of the samples were preconditioned with four formation cycles before the measurements. The fifth-cycle voltage profile with selected *ex situ* Fe1/3-2-4.3, Fe1/3-2-4, and Fe08-2-4 samples at different SOC are shown in Figure 3a–c, respectively. Fe1/

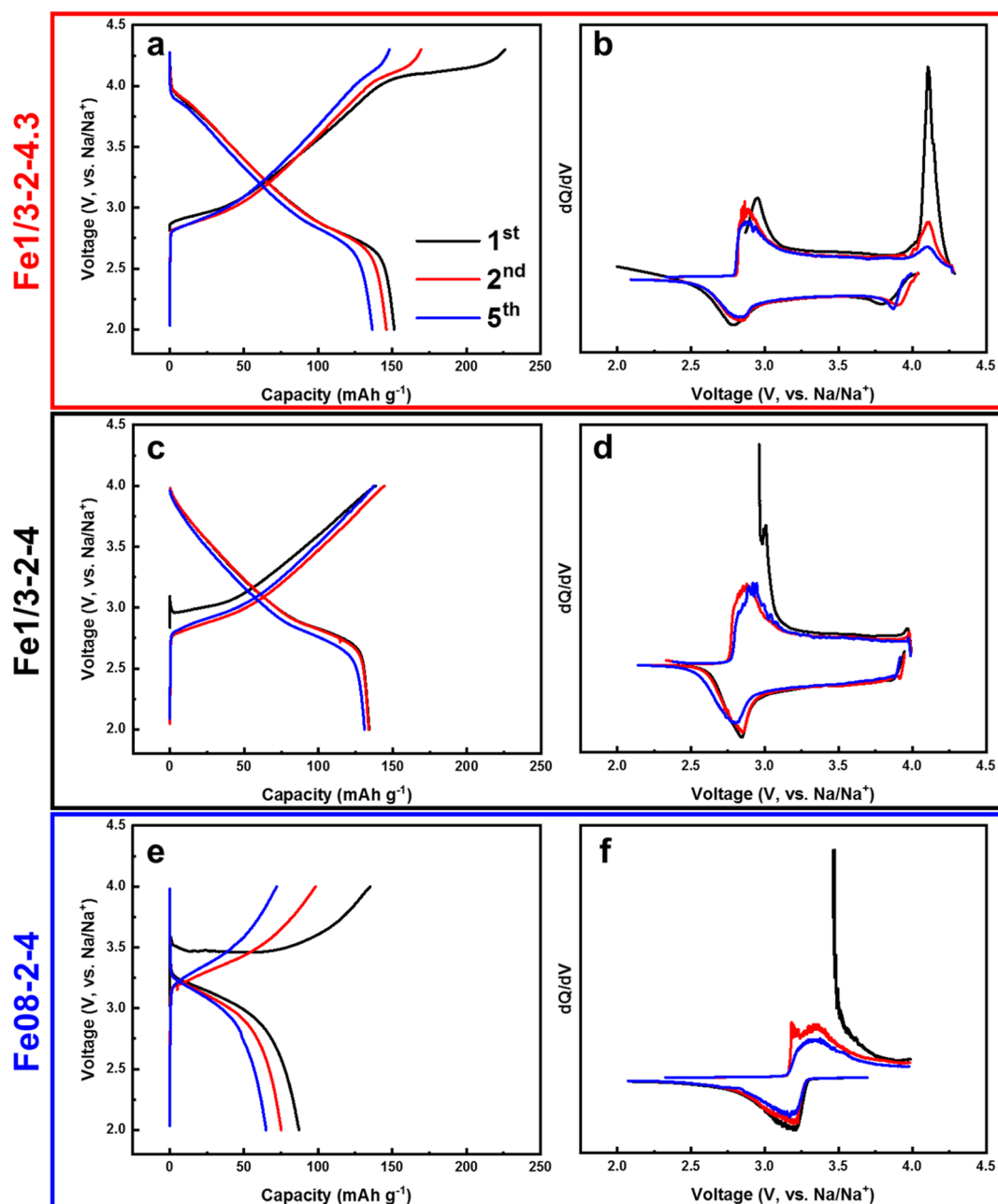


Figure 2. (a,c,e) Voltage profiles and (b,d,f) dQ/dV plots of (a,b) Fe1/3-2-4.3, (c,d) Fe1/3-2-4, and (e,f) Fe08-2-4 samples cycled at 12 mA g^{-1} .

3-2-4.3 and Fe1/3-2-4 are selected to explore the reversibility in different potential windows. In addition, Fe1/3-2-4 and Fe08-2-4 are used for investigation of TM composition effect.

K-edge XANES spectra of Mn (Figure 4a–c), Ni (Figure 4d–f), and Fe (Figure 4g–i) ions of Fe1/3-2-4.3 (Figure 4a,d,g), Fe1/3-2-4 (Figure 4b,e,h), and Fe08-2-4 (Figure 4c,f,i) samples are shown in Figure 4. The first strong absorption is related to the shake-down process from the ligand-to-metal charge transfer (LMCT).^{22,23} The primary absorption corresponds to the electric dipole-allowed transition from $1s$ to a $4p$ orbital.^{22,24}

Because the Mn K-edge position of pristine NFM-Fe_{1/3} and NFM-Fe_{0.8} samples is close to that of the standard MnO₂ instead of Mn₂O₃, the valence of Mn ions in both samples is assigned as tetravalent. Within each Fe1/3-2-4.3, Fe1/3-2-4, and Fe08-2-4 sample, the shape of Mn K-edge spectra changes

because of the evolution of the local environment.^{23,25} The edge position of *ex situ* Mn K-edge spectra does not have a clear shift to the high or low energy region during the charging or discharging process, indicating the electrochemically inactive feature of Mn⁴⁺ ions. Moreover, the valence of Mn ions can be determined by the intensity of the pre-edge.^{22,26} The negligible change of the pre-edge intensity of the *ex situ* Mn samples confirms that tetravalent Mn ions prevail during the Na (de)insertion.

In terms of Ni K-edge spectra, the pristine NFM-Fe_{1/3} and NFM-Fe_{0.8} samples closely resemble the standard NiO sample, indicating the existence of Ni²⁺ ions. The spectrum of a standard NiOOH is also provided for the reference of Ni³⁺ ions. The shift of the Ni edge can be quantitatively estimated by the energy of the first inflection point ($E_{0,\text{Ni}}$), as shown in Figure S5 (Supporting Information).^{27,28} The voltage versus

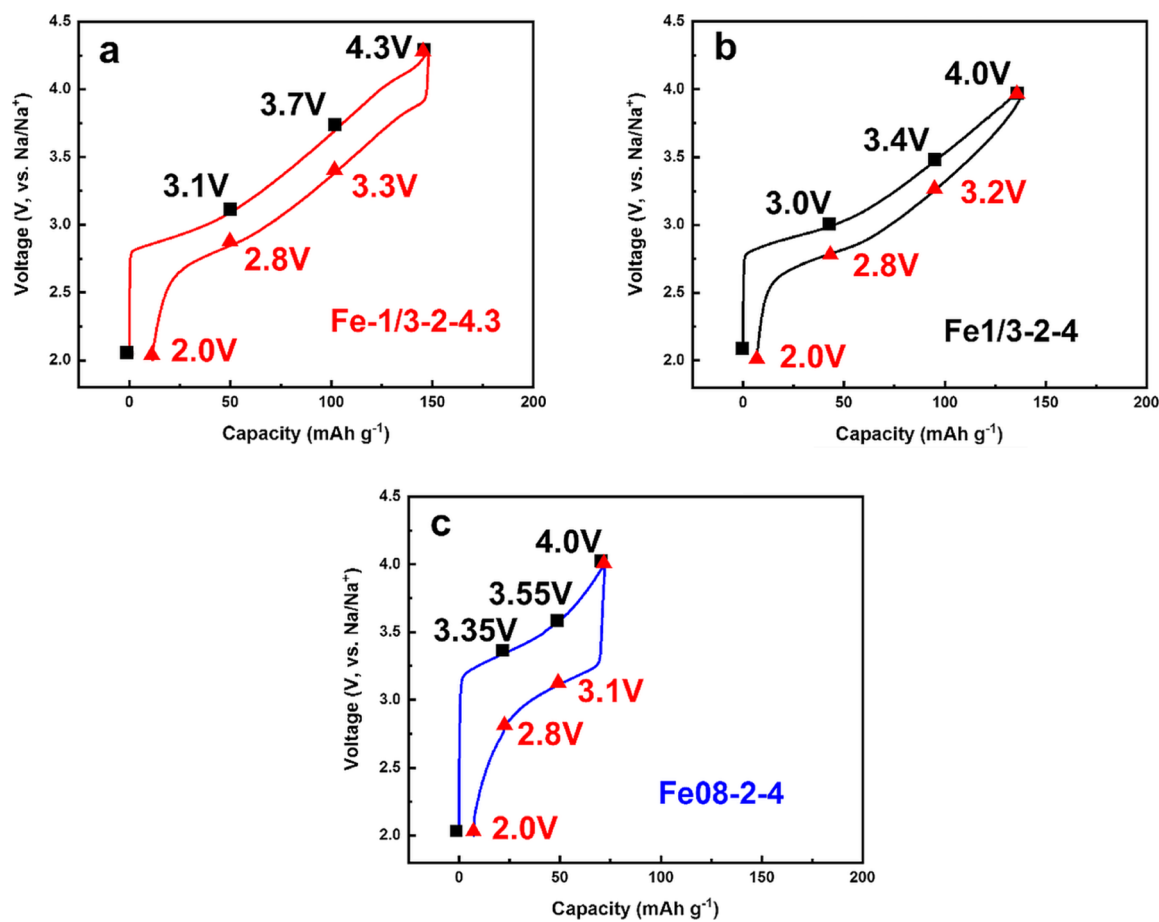


Figure 3. Fifth cycle voltage profiles of (a) Fe_{1/3}-2-4.3, (b) Fe_{1/3}-2-4, and (c) Fe₀₈-2-4 with the selected SOCs during cycling. The black squares and red triangles represent the voltage states during the charge and discharge process, respectively.

$E_{0,\text{Ni}}$ plots of Fe_{1/3}-2-4.3, Fe_{1/3}-2-4 and Fe₀₈-2-4 are shown in Figure 5a–c, respectively. In Fe_{1/3}-2-4 and Fe_{1/3}-2-4.3 samples, the $E_{0,\text{Ni}}$ value gradually increases and decreases during charge and discharge process, suggesting the oxidation and reduction of Ni ions, respectively. Moreover, the $E_{0,\text{Ni}}$ value at each charge/discharge step is similar to each other. All of above show a good reversibility of Fe_{1/3} samples at different potential windows during the cycling process. As for the Fe₀₈-2-4 sample, the oxidation state of Ni ions drastically increases from 3.4 to 4.0 V during the charge process, and it gradually decreases during the discharge process. It suggests that the Ni redox couple is active and contributes to the specific capacity. However, the E_0 of Ni ions does not return to the pristine state during discharge and a large irreversible behavior is observed during discharge, particularly at the low voltages. Because the Ni redox couple is quite reversible in the Fe_{1/3}-2-4 sample (Figure 5b) and because both Fe₀₈-2-4 and Fe_{1/3}-2-4 samples are cycled with the same potential window, the irreversibility of the nickel redox couple in the Fe₀₈-2-4 sample is possibly a result of the increase in Fe composition. Therefore, the Fe₀₈-2-4 sample shows limited electrochemical performance in terms of cycle life and rate capability (Figure 1).

As for Fe K-edge XANES spectra (Figure 4g–i), the shape and edge position of pristine NFM–Fe_{1/3} and NFM–Fe_{0.8} strongly resemble the standard Fe₂O₃ spectra, suggesting that trivalent Fe ions are present. For each sample, the edge positions of all curves at various voltages hardly shift during the

charging and discharging process, suggesting that Fe ions are barely electrochemically active after five precycle activation processes. Xie et al. reported an Fe³⁺/Fe⁴⁺ redox couple in the initial cycle of NaNi_{1/3}Fe_{1/3}Mn_{1/3}O₂ by XANES when charged above 4 V.⁹ The absence of the Fe³⁺/Fe⁴⁺ redox couple after the activation process demonstrates the irreversible electrochemical behavior of Fe ions. Lee et al. reported instability of the Fe³⁺/Fe⁴⁺ redox couple in α -NaFeO₂, where more than 20% of Fe⁴⁺ species that were generated in the desodiated Na_{1-x}FeO₂ electrode were spontaneously reduced back to Fe³⁺ during open circuit storage of the charged cell.¹⁶ This instability of Fe⁴⁺ may limit the sensitivity of the XANES measurement to detect the Fe⁴⁺ formed during cycling. As a result, Fe may be slightly more active than the XANES results would suggest. The samples were measured immediately after reaching the desired state of charge to minimize this effect. Additionally, the strong hybridization of bonding between Fe⁴⁺ and oxygen ligands could suppress the shift of the Fe K-edge XANES spectra upon oxidation from Fe³⁺ to Fe⁴⁺.^{29–33} Therefore, the irreversible specific capacity possibly results from the irreversible Fe³⁺/Fe⁴⁺ redox couple after cycles for all NFM layered cathodes.

We conducted *ex situ* EXAFS to examine the local structural evolution of each TM with different operating potential windows and TM composition. The Fourier-transformed magnitudes of Mn, Ni, and Fe EXAFS spectra of Fe_{1/3}-2-4.3 (Figure 6a,d,g), Fe_{1/3}-2-4 (Figure 6b,e,h), and Fe₀₈-2-4 (Figure 6c,f,i) samples are shown in Figure 6. The

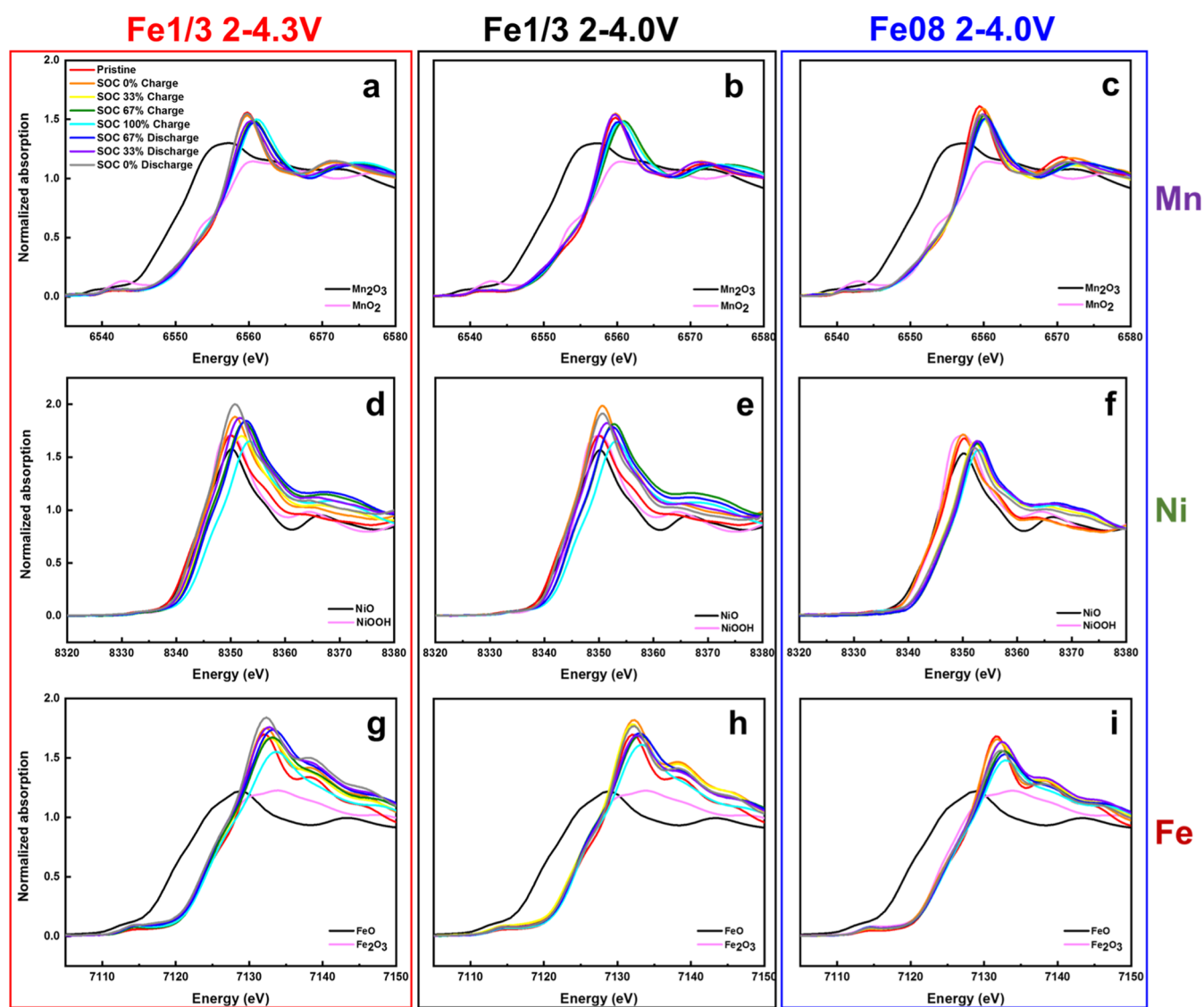


Figure 4. XANES K-edge spectra of (a–c) Mn, (d–f) Ni, and (g–i) Fe ions of (a,d,g) Fe_{1/3}-2-4.3, (b,e,h) Fe_{1/3}-2-4, and (c,f,i) Fe₀₈-2-4 sample. The data are collected at various voltages during fifth cycle corresponding to Figure 3.

first intense peak at a low radial distance is related to the TM–O first coordination shell, and the second one is related to TM–TM bonding.³⁴ Quantitative fitting of all *ex situ* EXAFS spectra is conducted (Table S3–S5, Supporting Information), and the plots of TM–O radial distance versus voltage are shown in Figure 7, where 7a to 7i correspond to 6a to 6i in Figure 6, respectively. The Mn–O distance in pristine NFM–Fe_{1/3} and NFM–Fe_{0.8} samples is 1.89 Å. Shiraishi et al. reported the radial distance of Mn⁴⁺–O in the octahedral coordination to be 1.88 Å,²⁸ and the theoretical distance of Mn⁴⁺–O calculated from the ionic radii is 1.91 Å.³⁵ Thus, it is believed that the Mn ions in all of pristine samples are tetravalent with octahedral coordination, in agreement with the XANES results (Figure 4a–c). The Mn–O distance at various SOC levels barely changes during Na⁺ insertion/extraction, which suggests that the local environment of Mn ions stays unaltered.

The Ni–O distance of the pristine NFM–Fe_{1/3} sample is 2.06 Å, which is smaller than that of the NFM–Fe_{0.8} sample at 2.08 Å. The larger Ni–O distance in the NFM–Fe_{0.8} sample corresponds to the expansion of the unit cell (Supporting Information, Table S1). Abraham et al. reported the Ni²⁺–O

and Ni⁴⁺–O distance in octahedral coordination to be 2.07 and 1.90 Å, respectively.³⁶ Therefore, the oxidation state of Ni ions is determined as divalent. Moreover, the Ni–O distances of Fe_{1/3}-2-4.3, Fe_{1/3}-2-4, and Fe₀₈-2-4 samples at the fully charged state are 1.92, 1.94, and 1.92 Å, respectively, all of which are close to the Ni⁴⁺–O distance of 1.90 Å, suggesting the activation of the Ni²⁺/Ni⁴⁺ redox couple. The Ni–O distance of Fe_{1/3}-2-4.3, Fe_{1/3}-2-4, and Fe₀₈-2-4 samples decreases during the charging process because of the oxidation of Ni ions (Figure 7a–c) and the shrinkage of the *a* lattice parameter as Na ions are extracted.³⁷ During the discharging process, the Ni–O distance in both NFM–Fe_{1/3} samples reversibly increases back to the fully discharged position (2.0 V). As for the discharging process of the Fe₀₈-2-4 sample, the Ni–O distance irreversibly decreases when the voltage is less than 3.1 V, resulting in the irreversibility in the low voltage region. Moreover, the Ni–O distance at 2.0 V keeps declining with cycles compared to that of the pristine sample, consistent with the evolution of the Ni oxidation state (Figure 5c). The irreversibility of the Fe₀₈-2-4 sample in the low potential

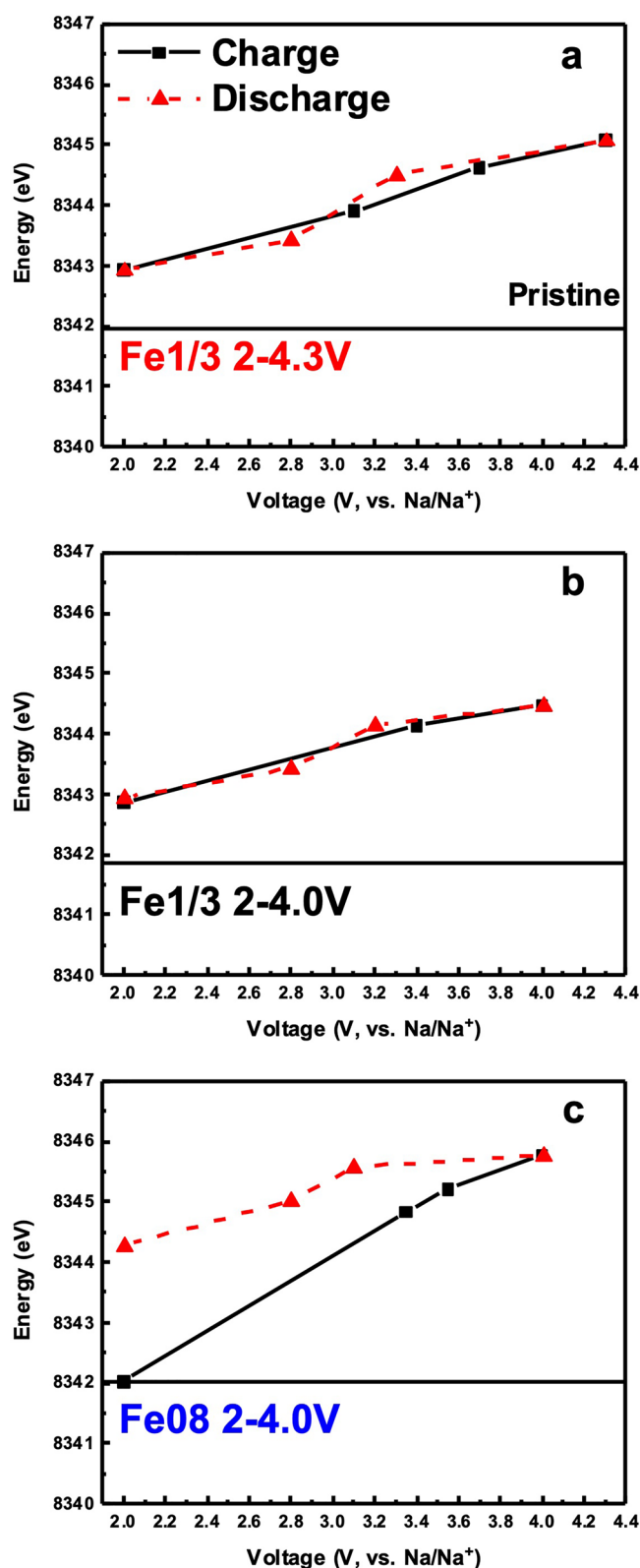


Figure 5. E_0 vs voltage plots based on Ni K-edge XANES spectra of (a) Fe_{1/3}-2-4.3, (b) Fe_{1/3}-2-4, and (c) Fe_{0.8}-2-4 samples.

region is demonstrated by both the Ni oxidation state and Ni–O distance.

The Fe–O distances in pristine NFM–Fe_{1/3} and NFM–Fe_{0.8} samples are both 2.02 Å. After the charging process, the Fe–O distance in Fe_{1/3}-2-4.3, Fe_{1/3}-2-4, and Fe_{0.8}-2-4 at

100% SOC decreases to 1.97, 1.98, and 1.96 Å, respectively. Yabuuchi et al. investigated the Fe³⁺/Fe⁴⁺ redox couple in the layered Na_x(Fe_{0.5}Mn_{0.5})O₂ cathode and observed that the Fe–O distances in the pristine and fully charged states at the first cycle were 2.00 and 1.90 Å, respectively.³² Then, the Fe³⁺/Fe⁴⁺ redox couple was confirmed by Mossbauer spectroscopy.³² In our case, the minor change in the Fe–O distance therefore can be interpreted as the distortion of the local lattice rather than redox behavior. It is consistent with XANES that Fe is inactive in the fifth cycle. During the discharging process, the Fe–O distance for all samples reversibly returns at 2.0 V, which is close to that at the pristine state.

Moreover, the plots of TM–TM radial distance versus voltage are shown in Figure 8, where 8a–i correspond to 6a–i in Figure 6, respectively. The TM–TM distance of all samples decreases during the charge process because of the decrease of the *a* lattice parameter, which is related to the in-plane interatomic distance.^{23,34} The distance increases during the discharging process. NFM–Fe_{1/3} samples cycled between both 2–4 and 2–4.3 V demonstrate great reversible evolution of the TM–TM distance. The distance of Mn–TM (Figure 8a,b), Ni–TM (Figure 8d,e), and Fe–TM (Figure 8g,h) bonds at the fully discharged state and fully charged state almost overlaps with the corresponding steps in the discharge process. As for the Fe_{0.8}-2-4 sample, however, there is a gap between the distance at SOC_{0%} of the charge and discharge process for Mn–TM (Figure 8c), Ni–TM (Figure 8f), and Fe–TM (Figure 8i). The Ni–TM distance shows the most significant gap among all TM–TM distances, suggesting the irreversibility largely results from the Ni redox couple, consistent with the XANES results.

The cumulative irreversible capacity loss in the first four cycles and the fifth cycle charge capacity is compared to the theoretical capacities based only on the Ni²⁺/Ni⁴⁺ redox couple for each voltage window and composition in Table 1. For all compositions, the theoretical capacity including both Ni and Fe redox couples is 240–241 mAh/g. Higher content of Fe and higher upper charge cutoff voltage in the potential window result in a greater irreversible extraction of Na in the first four cycles. The resulting fifth cycle charge capacity when compared to the theoretical capacity based only on the Ni²⁺/Ni⁴⁺ redox couple suggests that in the NFM–Fe_{0.8} and Fe_{0.5} samples, that the complete oxidation of all Ni²⁺ to the 4+ oxidation state could explain almost all of the observed charge capacity. For NFM–Fe_{1/3}, only partial oxidation of Ni²⁺ to an average oxidation state of ~3.6+ is necessary to explain the observed fifth cycle charge capacity. To compensate the irreversible Na extraction in the NFM–Fe_{0.5} and Fe_{0.8} samples, some of the Fe or Mn must oxidize. Mn is observed to be in the 4+ oxidation state in the pristine material and is inactive between cycles 1 and 5, so the Fe³⁺ may oxidize to Fe⁴⁺ to provide the compensation. Given the possibility of side reactions¹⁶ or oxygen redox³⁸ contributing to the charge capacity, the upper bound for the percentage of Fe as Fe⁴⁺ after the first four cycles can be calculated based on the irreversible Na extraction in these cycles. For example, the sample Fe_{0.5}-2-4 demonstrates 21.1 mA h/g of irreversible capacity in the first four cycles and has a theoretical capacity based only on Fe redox of 120.4 mA h/g. The ratio of these two values gives the maximum fraction of Fe that may exist as Fe⁴⁺, which is ~18% for Fe_{0.5}-2-4. Considering each sample, this value is ~5, 18, and 56% for NFM–Fe_{1/3}, Fe_{0.5}, and Fe_{0.8} in the 2–4 V range, respectively. In the 2–4.3 V range, the value is and ~52, 52, and 76% for

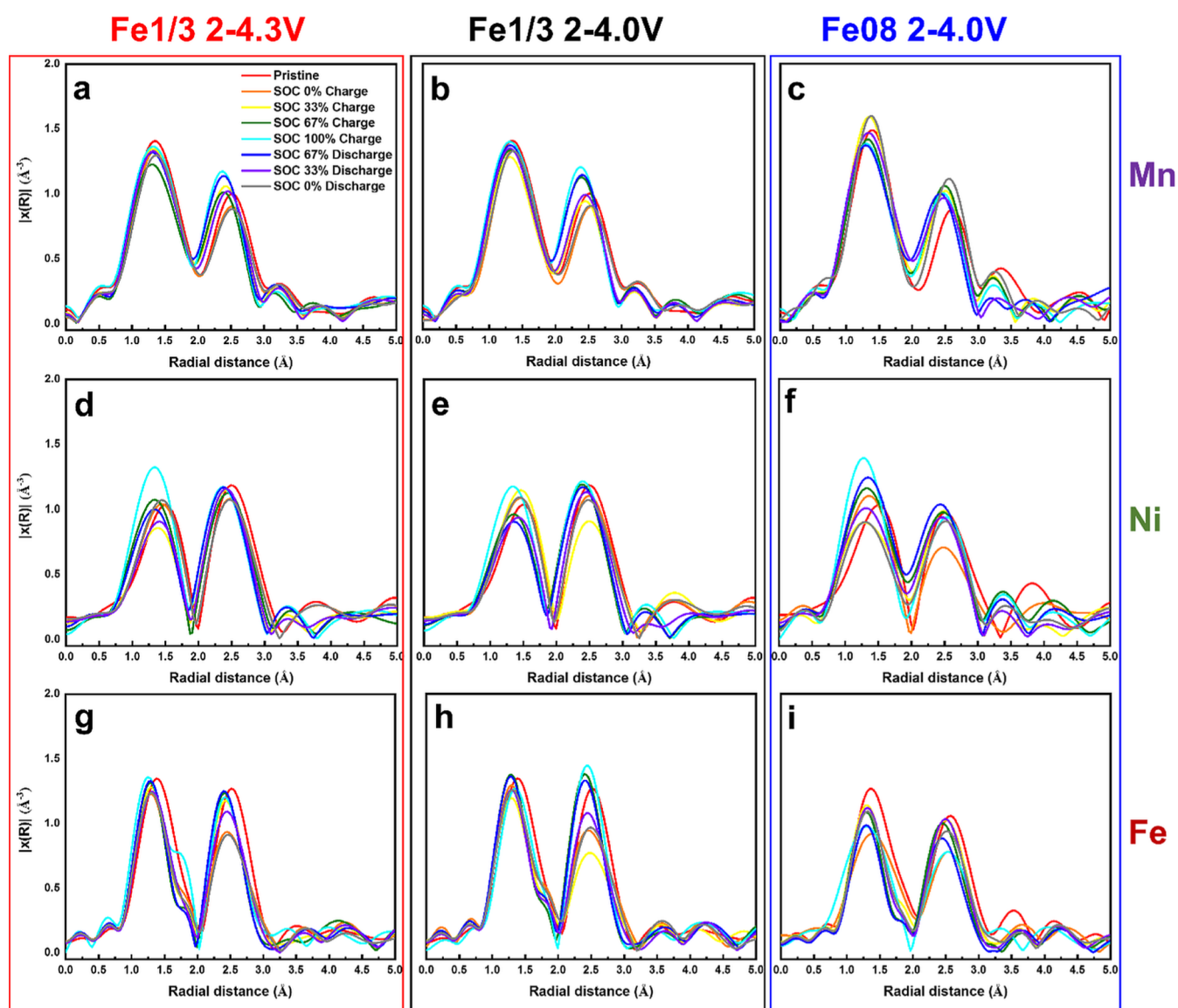


Figure 6. Fourier-transformed magnitude of EXAFS spectra (nonphase shift-corrected) of (a–c) Mn, (d–f) Ni, and (g–i) Fe ions of (a,d,g) Fe1/3-2-4.3, (b,e,h) Fe1/3-2-4, and (c,f,i) Fe0.8-2-4 samples. The data are collected at various voltages during fifth cycle corresponding to Figure 3.

NFM-Fe_{1/3}, Fe_{0.5}, and Fe_{0.8}, respectively. Lee et al. observed 40.2% of Fe as Fe⁴⁺ in NaFeO₂ when charged to 3.6 V. The P2-type Na_{2/3}Fe_{1/2}Mn_{1/2}O₂ was observed by Yabuuchi et al. to have 20% of Fe as Fe⁴⁺ when charged to 4.5 V.³⁹ Other than the obvious differences in composition, the relatively higher percentage of Fe⁴⁺ calculated in our Fe_{0.5} and Fe_{0.8} samples could be explained by the contribution of the three additional cycles that were undergone and the different voltage window. The samples with a higher fraction of Fe irreversibly oxidized in the first four cycles show greater instability of their remaining capacity from cycle 5–100, as shown in Figure S4 (Supporting Information). The presence of Fe³⁺ in highly desodiated O3–NaFeO₂ may suppress layer gliding associated with phase transitions by migrating from 3b sites to face-shared tetrahedral 6c sites, but the accumulation of Fe³⁺ on 6c sites over many cycles could cause structural disorder which lowers the discharge potential and blocks sodium reintercalation.¹⁶ The large voltage hysteresis seen in the fifth cycle for Fe0.8-2-4 (Figure 5c) could suggest such a mechanism is also active in the Fe_{0.8} system. The chemical instability of Fe⁴⁺ by reaction

with electrolyte¹⁶ or disproportionation reaction ($2\text{Fe}^{4+} \rightarrow \text{Fe}^{3+} + \text{Fe}^{5+}$)⁴ may further contribute to the capacity degradation of the samples with higher Fe content. Additionally, the low Ni:Fe ratio in the NFM-Fe_{0.5} and Fe_{0.8} sample reduces the stabilizing effect that LMCT between Ni and Fe can have by suppressing Fe⁴⁺ formation.⁴⁰

To develop a more complete understanding of the complex interactions between the Ni, Mn, and Fe ions in O3-type structures, further experimentation must be done to quantitatively identify Fe⁴⁺ formation over many cycles. Special attention to the influence of oxygen redox and side reactions is needed to separate these effects from the TM–TM interactions (especially between Fe and Ni), which are evident in the Fe0.8-2-4 V sample. Experiments designed with these considerations in mind will be the subject of future work. Methods for enhancing the reversibility of Fe-rich cathode materials such as TM substitution, surface engineering of the active material, and electrolyte additives are also of great interest for further research.⁴¹

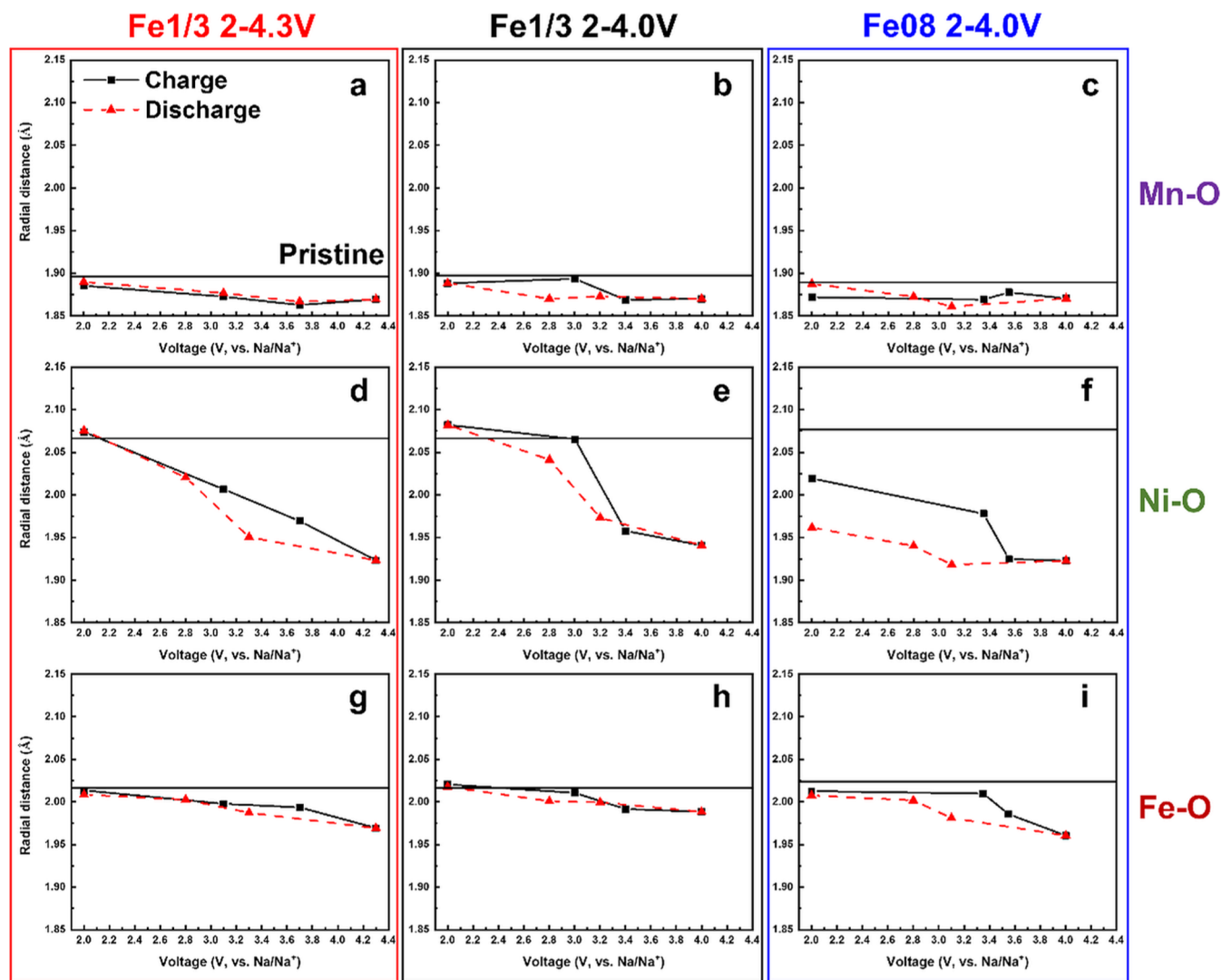


Figure 7. TM–O distance versus voltages plots of (a–c) Mn–O, (d–f) Ni–O, and (g–i) Fe–O ions of (a,d,g) Fe_{1/3}-2-4.3, (b,e,h) Fe_{1/3}-2-4, and (c,f,i) Fe_{0.8}-2-4 samples. The data are derived from the EXAFS spectra in Figure 6.

4. CONCLUSIONS

We prepared NFM–Fe_{1/3}, NFM–Fe_{0.5}, and NFM–Fe_{0.8} to study the reversibility of the TM valence and bonding distance in various cation compositions and different operation potential windows. The crystalline structure of Na–Ni_yFe_xMn_yO₂ cathodes is investigated by XRD and Rietveld refinement, where the O3-type layered α -NaFeO₂ structure (space group: $R\bar{3}m$) is obtained. The electrochemical performance, for example, rate capability and cycle life of the samples becomes limited with the increase of either Fe content or the upper charge cutoff potential. This may be associated with the irreversible oxidation of some or most of Fe³⁺ to Fe⁴⁺, which can destabilize O3-type materials. *Ex situ* synchrotron XANES and EXAFS of precycled samples are conducted to observe the TM valence and bonding evolution. The oxidation state of Mn ions in all three samples does not undergo significant change during the fifth charge/discharge processes, suggesting its electrochemically inactive behavior. The Fe³⁺/Fe⁴⁺ redox couple was observed in the initial cycle in a previous report.⁹ However, it becomes electrochemically inactive after five precycle activation processes, suggesting irreversibility of the Fe³⁺/Fe⁴⁺ redox couple. As for the Ni redox couple, it

contributes the most specific capacity for all three samples. Both Fe_{1/3}-2-4 and Fe_{1/3}-2-4.3 samples show great reversibility during the activation process and the charge/discharge process in fifth cycle. However, there is a large irreversibility of the Ni redox couple in the Fe_{0.8}-2-4 sample with cycles. As for the local TM–O bonding structure, Mn–O and Fe–O bond distances barely change upon cycling. Ni–O bonding exhibits great reversibility in the Na–Ni_{1/3}Fe_{1/3}Mn_{1/3}O₂ cathode in both potential windows. However, the Ni–O bond distance changes irreversibly at the low potential region in an Fe-rich cathode, consistent with the Ni valence evolution. Moreover, the TM–TM distances, including Ni–TM, Mn–TM, and Fe–TM, in the Na–Ni_{1/3}Fe_{1/3}Mn_{1/3}O₂ cathode reversibly expand and contract when cycled in both potential windows. However, in the Fe-rich cathode, the evolution of all TM–TM distances becomes irreversible, particularly for Ni–TM distance. In summary, it is found that Mn ions are electrochemically inactive in NaNi_xFe_yMn_zO₂ cathodes. The Fe redox couple is inactive after the five precycle activation processes. The Ni redox couple is quite reversible in the NaNi_xFe_yMn_zO₂ cathode when Fe content is low. However, it shows significant irreversibility when Fe content is high (up to 0.8). It suggests that the

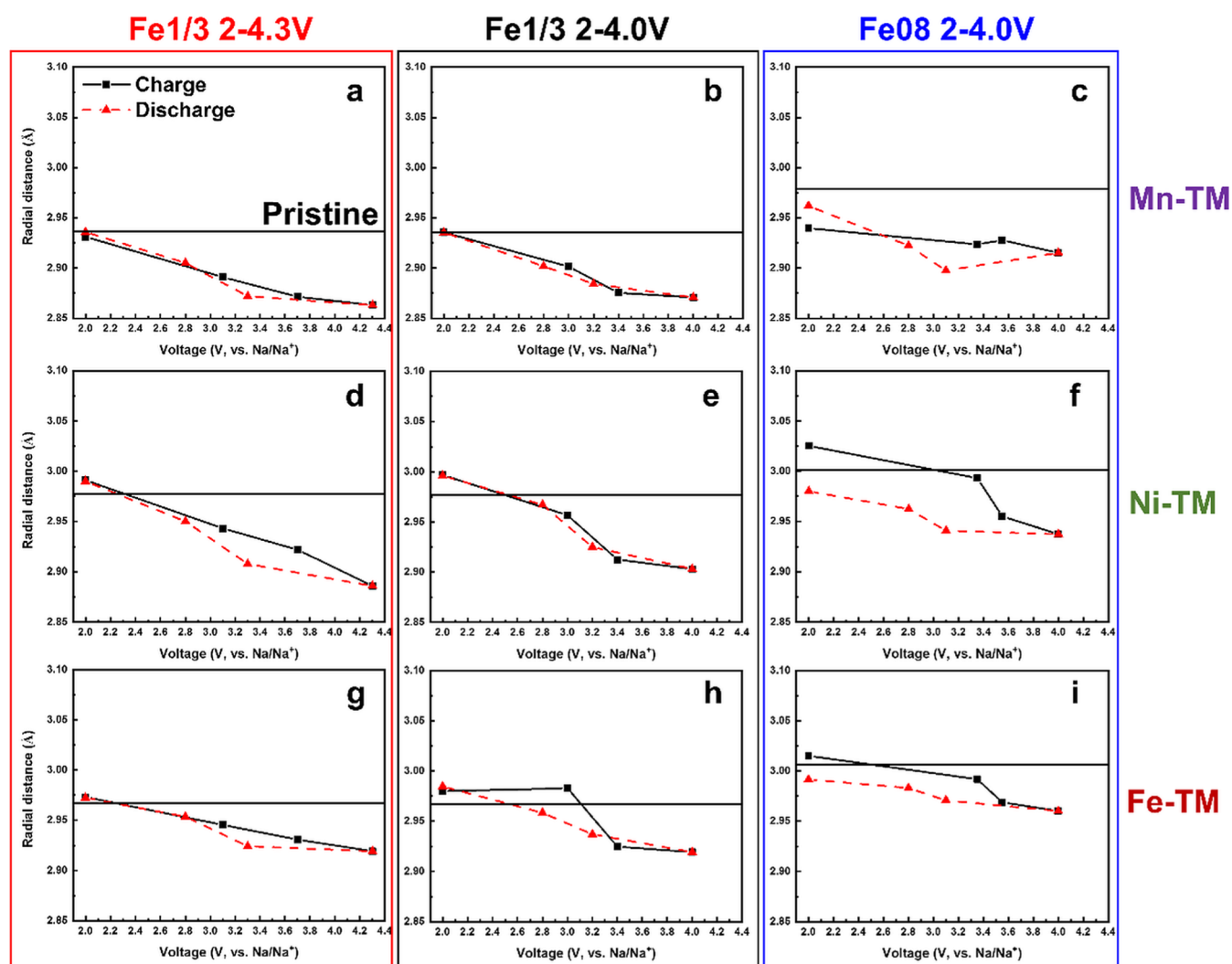


Figure 8. Voltages versus TM–TM distance plots of (a–c) Mn–TM, (d–f) Ni–TM, and (g–i) Fe–TM ions of (a,d,g) Fe_{1/3}-2-4.3, (b,e,h) Fe_{1/3}-2-4, and (c,f,i) Fe_{0.8}-2-4 samples. The data are derived from the EXAFS spectra in Figure 6.

Table 1. Cumulative Irreversible Capacity in First Four Cycles and Comparison between the Fifth Cycle Charge Capacity and Theoretical Capacities Based Only on the Ni²⁺/Ni⁴⁺ Redox Couple^a

sample	First four cycles irreversible capacity (mA h/g)	Fifth cycle charge capacity (mA h/g)	theoretical capacity with Ni ²⁺ /Ni ⁴⁺ redox only (mA h/g)	Fifth cycle charge capacity ratio to theoretical capacity with Ni redox only (%)
Fe _{1/3} -2-4	4.4	125.1	160.3	78.1
Fe _{0.5} -2-4	21.1	110.4	120.4	91.7
Fe _{0.8} -2-4	107.3	47.0	48.3	97.3
Fe _{1/3} -2-4.3	41.7	131.5	160.3	82.0
Fe _{0.5} -2-4.3	62.6	116.7	120.4	96.9
Fe _{0.8} -2-4.3	147.5	46.4	48.3	96.1

^aData are derived from Figure 1b.

irreversibility in the NaNi_xFe_yMn_zO₂ cathode possibly results from the irreversible Fe redox couple in the activation cycles, which harms the reversibility of the Ni redox couple in Fe-rich cathodes.

ASSOCIATED CONTENT

Supporting Information

The Supporting Information is available free of charge at <https://pubs.acs.org/doi/10.1021/acsami.0c13850>.

SEM of NFM–Fe_{1/3}, NFM–Fe_{0.5}, and NFM–Fe_{0.8}; XRD of NFM samples; refined unit cell parameters of NFM samples as a function of iron content; capacity retention (%) after cycle 5 of NFM samples; and tables of Reitveld refinement results; tables of Ni, Fe, and Mn EXAFS fitting results and first inflection point energies (PDF)

AUTHOR INFORMATION

Corresponding Authors

Eungje Lee – Chemical Sciences and Engineering Division, Argonne National Laboratory, Argonne, Illinois 60439, United States; orcid.org/0000-0003-3647-1595; Email: eungje.lee@anl.gov

Hui Xiong – Micron School of Materials Science and Engineering, Boise State University, Boise, Idaho 83725, United States; Center for Advanced Energy Studies (CAES), Idaho Falls, Idaho 83401, United States; orcid.org/0000-0003-3126-1476; Email: clairexiong@boisestate.edu

Authors

Changjian Deng – Micron School of Materials Science and Engineering, Boise State University, Boise, Idaho 83725, United States

Eric Gabriel – Micron School of Materials Science and Engineering, Boise State University, Boise, Idaho 83725, United States

Paige Skinner – Micron School of Materials Science and Engineering, Boise State University, Boise, Idaho 83725, United States

Sungsik Lee – X-ray Science Division, Argonne National Laboratory, Argonne, Illinois 60439, United States;
orcid.org/0000-0002-1425-9852

Pete Barnes – Micron School of Materials Science and Engineering, Boise State University, Boise, Idaho 83725, United States

Chunrong Ma – Micron School of Materials Science and Engineering, Boise State University, Boise, Idaho 83725, United States

Jihyeon Gim – Chemical Sciences and Engineering Division, Argonne National Laboratory, Argonne, Illinois 60439, United States

Miu Lun Lau – Micron School of Materials Science and Engineering, Boise State University, Boise, Idaho 83725, United States

Complete contact information is available at:
<https://pubs.acs.org/10.1021/acsami.0c13850>

Notes

The authors declare no competing financial interest.

ACKNOWLEDGMENTS

This material is based upon work supported by the U.S. Department of Energy, Office of Science, Office of Basic Energy Sciences program under Award Number DE-SC0019121. This research used resources of the Advanced Photon Source, a U.S. Department of Energy (DOE) Office of Science User Facility operated for the DOE Office of Science by the Argonne National Laboratory under Contract no. DE-AC02-06CH11357. The work by J.G. and E.L. was supported by the Advanced Battery Materials Research (BMR) Program of the U.S. Department of Energy, Office of Energy Efficiency and Renewable Energy.

REFERENCES

- (1) Slater, M. D.; Kim, D.; Lee, E.; Johnson, C. S. Sodium-ion Batteries. *Adv. Funct. Mater.* **2013**, *23*, 947–958.
- (2) Kundu, D.; Talaie, E.; Duffort, V.; Nazar, L. F. The Emerging Chemistry of Sodium Ion Batteries for Electrochemical Energy Storage. *Angew. Chem., Int. Ed.* **2015**, *54*, 3431–3448.
- (3) Xiang, X.; Zhang, K.; Chen, J. Recent Advances and Prospects of Cathode Materials for Sodium-ion Batteries. *Adv. Mater.* **2015**, *27*, 5343–5364.
- (4) Yabuuchi, N.; Kubota, K.; Dahbi, M.; Komaba, S. Research Development on Sodium-Ion Batteries. *Chem. Rev.* **2014**, *114*, 11636–11682.
- (5) Kim, S.-W.; Seo, D.-H.; Ma, X.; Ceder, G.; Kang, K. Electrode Materials for Rechargeable Sodium-Ion Batteries: Potential Alternatives to Current Lithium-Ion Batteries. *Adv. Energy Mater.* **2012**, *2*, 710–721.
- (6) Yabuuchi, N.; Yano, M.; Yoshida, H.; Kuze, S.; Komaba, S. Synthesis and Electrode Performance of O3-Type NaFeO₂-NaNi_{1/2}Mn_{1/2}O₂ Solid Solution for Rechargeable Sodium Batteries. *J. Electrochem. Soc.* **2013**, *160*, A3131–A3137.

(7) Yuan, D. D.; Wang, Y. X.; Cao, Y. L.; Ai, X. P.; Yang, H. X. Improved Electrochemical Performance of Fe-Substituted NaNi_{0.5}Mn_{0.5}O₂ Cathode Materials for Sodium-Ion Batteries. *ACS Appl. Mater. Interfaces* **2015**, *7*, 8585–8591.

(8) Wang, H.; Liao, X.-Z.; Yang, Y.; Yan, X.; He, Y.-S.; Ma, Z.-F. Large-Scale Synthesis of NaNi_{1/3}Fe_{1/3}Mn_{1/3}O₂ as High Performance Cathode Materials for Sodium Ion Batteries. *J. Electrochem. Soc.* **2016**, *163*, A565–A570.

(9) Xie, Y.; Wang, H.; Xu, G.; Wang, J.; Sheng, H.; Chen, Z.; Ren, Y.; Sun, C.-J.; Wen, J.; Wang, J.; Miller, D. J.; Lu, J.; Amine, K.; Ma, Z.-F. In Operando XRD and TXM Study on the Metastable Structure Change of NaNi_{1/3}Fe_{1/3}Mn_{1/3}O₂ under Electrochemical Sodium-Ion Intercalation. *Adv. Energy Mater.* **2016**, *6*, 1601306.

(10) Kang, B.; Ceder, G. Battery Materials for Ultrafast Charging and Discharging. *Nature* **2009**, *458*, 190–193.

(11) Kang, K.; Meng, Y. S.; Bréger, J.; Grey, C. P.; Ceder, G. Electrodes with High Power and High Capacity for Rechargeable Lithium Batteries. *Science* **2006**, *311*, 977–980.

(12) Liu, C.; Neale, Z. G.; Cao, G. Understanding Electrochemical Potentials of Cathode Materials in Rechargeable Batteries. *Mater. Today* **2016**, *19*, 109–123.

(13) Li, Y.; Zhang, R.; Huang, Y. Air-Stable Copper-Based P2-Na_{7/9}Cu_{2/9}Fe_{1/9}Mn_{2/3}O₂ as a New Positive Electrode Material for Sodium-Ion Batteries. *Front. Chem.* **2015**, *2*, 1500031.

(14) Yao, H.-R.; Wang, P.-F.; Gong, Y.; Zhang, J.; Yu, X.; Gu, L.; OuYang, C.; Yin, Y.-X.; Hu, E.; Yang, X.-Q.; Stavitski, E.; Guo, Y.-G.; Wan, L.-J. Designing Air-Stable O3-Type Cathode Materials by Combined Structure Modulation for Na-Ion Batteries. *J. Am. Chem. Soc.* **2017**, *139*, 8440–8443.

(15) Wang, P.-F.; You, Y.; Yin, Y.-X.; Guo, Y.-G. Layered Oxide Cathodes for Sodium-Ion Batteries: Phase Transition, Air Stability, and Performance. *Adv. Energy Mater.* **2018**, *8*, 1701912.

(16) Lee, E.; Brown, D. E.; Alp, E. E.; Ren, Y.; Lu, J.; Woo, J.-J.; Johnson, C. S. New Insights into the Performance Degradation of Fe-Based Layered Oxides in Sodium-Ion Batteries: Instability of Fe³⁺/Fe⁴⁺ Redox in α -NaFeO₂. *Chem. Mater.* **2015**, *27*, 6755–6764.

(17) Toby, B. H. EXPGUI, a Graphical User Interface for GSAS. *J. Appl. Crystallogr.* **2001**, *34*, 210–213.

(18) Newville, M. IFEFIT: Interactive XAFS Analysis and It FEFF Fitting. *J. Synchrotron Radiat.* **2001**, *8*, 322–324.

(19) Cabana, J.; Kwon, B. J.; Hu, L. Mechanisms of Degradation and Strategies for the Stabilization of Cathode–Electrolyte Interfaces in Li-Ion Batteries. *Acc. Chem. Res.* **2018**, *51*, 299–308.

(20) Zheng, L.; Li, L.; Shunmugasundaram, R.; Obrovac, M. N. Effect of Controlled-Atmosphere Storage and Ethanol Rinsing on NaNi_{0.5}Mn_{0.5}O₂ for Sodium-Ion Batteries. *ACS Appl. Mater. Interfaces* **2018**, *10*, 38246–38254.

(21) Myeong, S.; Cho, W.; Jin, W.; Hwang, J.; Yoon, M.; Yoo, Y.; Nam, G.; Jang, H.; Han, J.-G.; Choi, N.-S. Understanding Voltage Decay in Lithium-Excess Layered Cathode Materials through Oxygen-Centred Structural Arrangement. *Nat. Commun.* **2018**, *9*, 3285.

(22) Ito, A.; Sato, Y.; Sanada, T.; Hatano, M.; Horie, H.; Ohsawa, Y. In Situ X-Ray Absorption Spectroscopic Study of Li-Rich Layered Cathode Material Li [Ni_{0.17}Li_{0.2}Co_{0.07}Mn_{0.56}]O₂. *J. Power Sources* **2011**, *196*, 6828–6834.

(23) Komaba, S.; Yabuuchi, N.; Nakayama, T.; Ogata, A.; Ishikawa, T.; Nakai, I. Study on the Reversible Electrode Reaction of Na_{1-x}Ni_{0.5}Mn_{0.5}O₂ for a Rechargeable Sodium-Ion Battery. *Inorg. Chem.* **2012**, *51*, 6211–6220.

(24) Yoon, W.-S.; Balasubramanian, M.; Chung, K. Y.; Yang, X.-Q.; McBreen, J.; Grey, C. P.; Fischer, D. A. Investigation of the Charge Compensation Mechanism on the Electrochemically Li-Ion Deintercalated Li_{1-x}Co_{1/3}Ni_{1/3}Mn_{1/3}O₂ Electrode System by Combination of Soft and Hard X-Ray Absorption Spectroscopy. *J. Am. Chem. Soc.* **2005**, *127*, 17479–17487.

(25) Yue, J.-L.; Yin, W.-W.; Cao, M.-H.; Zulipiya, S.; Zhou, Y.-N.; Fu, Z.-W. A Quinary Layer Transition Metal Oxide of NaNi_{1/4}Co_{1/4}Fe_{1/4}Mn_{1/8}Ti_{1/8}O₂ as a High-Rate-Capability and Long-

Cycle-Life Cathode Material for Rechargeable Sodium Ion Batteries. *Chem. Commun.* **2015**, *51*, 15712–15715.

(26) Croy, J. R.; Gallagher, K. G.; Balasubramanian, M.; Chen, Z.; Ren, Y.; Kim, D.; Kang, S.-H.; Dees, D. W.; Thackeray, M. M. Examining Hysteresis in Composite x $\text{Li}_2\text{MnO}_3 \cdot (1-x)$ LiMO_2 Cathode Structures. *J. Phys. Chem. C* **2013**, *117*, 6525–6536.

(27) Kuppan, S.; Duncan, H.; Chen, G. Controlling Side Reactions and Self-Discharge in High-Voltage Spinel Cathodes: The Critical Role of Surface Crystallographic Facets. *Phys. Chem. Chem. Phys.* **2015**, *17*, 26471–26481.

(28) Hu, E.; Bak, S.-M.; Liu, J.; Yu, X.; Zhou, Y.; Ehrlich, S. N.; Yang, X.-Q.; Nam, K.-W. Oxygen-Release-Related Thermal Stability and Decomposition Pathways of $\text{Li}_x\text{Ni}_{0.5}\text{Mn}_{1.5}\text{O}_4$ Cathode Materials. *Chem. Mater.* **2014**, *26*, 1108–1118.

(29) Abbate, M.; de Groot, F. M. F.; Fuggle, J. C.; Fujimori, A.; Strebel, O.; Lopez, F.; Domke, M.; Kaindl, G.; Sawatzky, G. A.; Takano, M.; Takeda, Y.; Eisaki, H.; Uchida, S. Controlled-Valence Properties of $\text{La}_{1-x}\text{Sr}_x\text{FeO}_3$ and $\text{La}_{1-x}\text{Sr}_x\text{MnO}_3$ Studied by Soft-x-Ray Absorption Spectroscopy. *Phys. Rev. B: Condens. Matter Mater. Phys.* **1992**, *46*, 4511.

(30) Suntivich, J.; Hong, W. T.; Lee, Y.-L.; Rondinelli, J. M.; Yang, W.; Goodenough, J. B.; Dabrowski, B.; Freeland, J. W.; Shao-Horn, Y. Estimating Hybridization of Transition Metal and Oxygen States in Perovskites from Ok-Edge x-Ray Absorption Spectroscopy. *J. Phys. Chem. C* **2014**, *118*, 1856–1863.

(31) Frati, F.; Hunault, M. O. J. Y.; de Groot, F. M. F. Oxygen K-Edge X-Ray Absorption Spectra. *Chem. Rev.* **2020**, *120*, 4056–4110.

(32) Shen, Z.; Zhuang, Y.; Li, W.; Huang, X.; Oropeza, F. E.; Hensen, E. J. M.; Hofmann, J. P.; Cui, M.; Tadich, A.; Qi, D.; Cheng, J.; Li, J.; Zhang, K. H. L. Increased Activity in the Oxygen Evolution Reaction by Fe 4+-Induced Hole States in Perovskite $\text{La}_{1-x}\text{Sr}_x\text{FeO}_3$. *J. Mater. Chem. A* **2020**, *8*, 4407–4415.

(33) González-Flores, D.; Klingan, K.; Chernev, P.; Loos, S.; Mohammadi, M. R.; Pasquini, C.; Kubella, P.; Zaharieva, I.; Smith, R. D. L.; Dau, H. Nickel-Iron Catalysts for Electrochemical Water Oxidation—Redox Synergism Investigated by in Situ X-Ray Spectroscopy with Millisecond Time Resolution. *Sustainable Energy Fuels* **2018**, *2*, 1986–1994.

(34) Deng, C.; Skinner, P.; Liu, Y.; Sun, M.; Tong, W.; Ma, C.; Lau, M. L.; Hunt, R.; Barnes, P.; Xu, J.; Xiong, H. Li-Substituted Layered Spinel Cathode Material for Sodium Ion Batteries. *Chem. Mater.* **2018**, *30*, 8145–8154.

(35) Shannon, R. D. Revised Effective Ionic Radii and Systematic Studies of Interatomic Distances in Halides and Chalcogenides. *Acta Crystallogr. A* **1976**, *32*, 751–767.

(36) Abraham, F.; Minaud, S.; Renard, C. Preliminary Crystal Structure of Mixed-Valency $\text{Sr}_4\text{Ni}_3\text{O}_9$, the Actual Formula of the so-Called $\text{Sr}_5\text{Ni}_4\text{O}_{11}$. *J. Mater. Chem.* **1994**, *4*, 1763–1764.

(37) Li, X.; Wu, D.; Zhou, Y.-N.; Liu, L.; Yang, X.-Q.; Ceder, G. O₃-Type $\text{Na}(\text{Mn}_{0.25}\text{Fe}_{0.25}\text{Co}_{0.25}\text{Ni}_{0.25})\text{O}_2$: A Quaternary Layered Cathode Compound for Rechargeable Na Ion Batteries. *Electrochem. Commun.* **2014**, *49*, 51–54.

(38) Li, Y.; Gao, Y.; Wang, X.; Shen, X.; Kong, Q.; Yu, R.; Lu, G.; Wang, Z.; Chen, L. Iron Migration and Oxygen Oxidation during Sodium Extraction from NaFeO_2 . *Nano Energy* **2018**, *47*, 519–526.

(39) Yabuuchi, N.; Kajiyama, M.; Iwatate, J.; Nishikawa, H.; Hitomi, S.; Okuyama, R.; Usui, R.; Yamada, Y.; Komaba, S. P₂-Type $\text{Na}_x[\text{Fe}_{1/2}\text{Mn}_{1/2}]\text{O}_2$ Made from Earth-Abundant Elements for Rechargeable Na Batteries. *Nat. Mater.* **2012**, *11*, 512–517.

(40) Wang, X.; Liu, G.; Iwao, T.; Okubo, M.; Yamada, A. Role of Ligand-to-Metal Charge Transfer in O₃-Type NaFeO_2 – NaNiO_2 Solid Solution for Enhanced Electrochemical Properties. *J. Phys. Chem. C* **2014**, *118*, 2970–2976.

(41) Xu, G.-L.; Amine, R.; Abouimrane, A.; Che, H.; Dahbi, M.; Ma, Z.-F.; Saadoune, I.; Alami, J.; Mattis, W. L.; Pan, F.; Chen, Z.; Amine, K. Challenges in Developing Electrodes, Electrolytes, and Diagnostics Tools to Understand and Advance Sodium-ion Batteries. *Adv. Energy Mater.* **2018**, *8*, 1702403.